



# Simplify your imaging workflows

**Make research imaging workflows accessible, traceable,  
and secure with Athena Software for Core Imaging Facilities.**

Thermo Scientific™ Athena Software is a premium imaging data management platform designed for core imaging facilities that support materials science research.

Athena Software ensures traceability of images, metadata, and experimental workflows through an intuitive and collaborative web interface.

Find out more at [thermofisher.com/athena](https://thermofisher.com/athena)

**ThermoFisher**  
SCIENTIFIC

# Multifunctional Self-Charging Electrochromic Supercapacitors Driven by Direct-Current Triboelectric Nanogenerators

Wenbin Guo, Zifeng Cong, Zi Hao Guo, Panpan Zhang, Yanghui Chen, Weiguo Hu,\*  
Zhong Lin Wang,\* and Xiong Pu\*

Electrochromic supercapacitor devices (ESCDs) are highly promising for energy-saving applications or smart windows, whereas they still require electrical energy inputs. In this study, a self-charging ESCD (SC-ESCD) based on the ESCD and a sliding-mode direct-current triboelectric nanogenerators is successfully proposed. The SC-ESCD cannot merely convert mechanical sliding kinetic energy into electrical energy and store the electricity in electrochromic supercapacitors but can also show optical responses to the mechanical sliding motions. The prominent electrochemical performances of the SC-ESCD are confirmed by the high areal capacitance ( $15.2 \text{ mF cm}^{-2}$  at  $0.1 \text{ mA cm}^{-2}$ ) and stable cycling performance (99% for 5000 cycles). Besides, it can be prepared into arbitrary characters or patterns to adapt to various applications. The study demonstrates a potential approach to develop multifunctional self-charging power sources which combine energy harvesting, energy storage, and electrochromic functions.

electrochromic supercapacitors have been reported with excellent electrochemical performances and potentially real-time indication of the energy level by their colors.<sup>[15,16]</sup> Moreover, the solar radiation transmittance can be modulated by electrochromic windows to control the room temperature, which is very promising for improving the energy efficiency of buildings.<sup>[17–22]</sup> Hence, intelligent electrochromic energy storage devices are highly desirable for their multiple applications.<sup>[23,24]</sup>

Electrochromic supercapacitor devices (ESCDs) are electro-responsive, which still require electrical stimuli or electrical energy inputs.<sup>[25–28]</sup> It would be ideal if an electricity generation device and the ESCDs can be integrated together. In this way, the sustainable energy sources can

be harvested and stored in ESCDs, and meantime they could trigger the optical responses of the ESCDs. Therefore, the ESCDs can respond to other stimuli and serve as a self-powered energy device as well. Triboelectric nanogenerator (TENG) has been proven to be able to convert mechanical energy from the environment or human motion into electricity.<sup>[29,30]</sup> Compared with photovoltaic and thermoelectric energy harvesting, mechanical energy is hardly affected by the weather and the working environment.<sup>[31,32]</sup> Preliminary progress have also been made to integrate TENG with energy storage device for self-charging power sources.<sup>[14,15,33,34]</sup> Nevertheless, the alternating current output of the TENG makes the redundant and rigid

## 1. Introduction

Electrochromic devices have been widely utilized in various applications, such as smart windows, information displays, and anti-glare mirrors.<sup>[1–4]</sup> Many electrochromic species can also be used as energy storage active materials, including metal oxides ( $\text{WO}_3$ ,  $\text{V}_2\text{O}_5$ ,  $\text{NiO}$ ), hexacyanometal salts ( $[\text{Fe}^{\text{III}}\text{Fe}^{\text{II}}(\text{CN})_6]^-$ ), viologen (bipyridilium compounds) and conjugated polymers, due to the fact that their characteristic color change is induced by electrochemical reactions.<sup>[5–10]</sup> Therefore, dual-function devices have been reported to serve simultaneously as both electrochromic and energy storage devices.<sup>[11–14]</sup> In particular,


W. Guo, Z. Cong, Z. H. Guo, Dr. P. Zhang, Dr. Y. Chen, Prof. W. Hu,  
Prof. Z. L. Wang, Prof. X. Pu  
CAS Center for Excellence in Nanoscience  
Beijing Key Laboratory of Micro-Nano Energy and Sensor  
Beijing Institute of Nanoenergy and Nanosystems  
Chinese Academy of Sciences  
Beijing 100083, China  
E-mail: huweiguo@binn.cas.cn; puxiong@binn.cas.cn

W. Guo, Z. Cong, Z. H. Guo, Dr. P. Zhang, Dr. Y. Chen, Prof. W. Hu,  
Prof. Z. L. Wang, Prof. X. Pu  
School of Nanoscience and Technology  
University of Chinese Academy of Sciences  
Beijing 100049, China

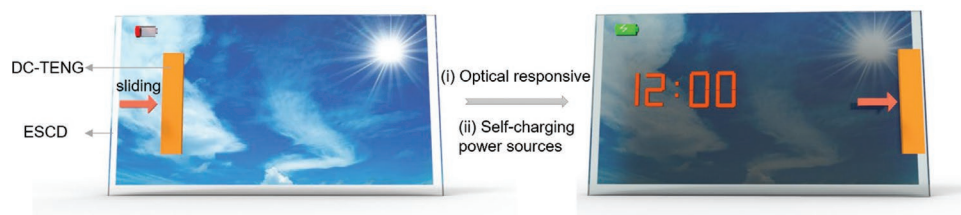
Prof. W. Hu, Prof. X. Pu  
Center on Nanoenergy Research  
School of Chemistry and Chemical Engineering  
School of Physical Science and Technology  
Guangxi University  
Nanning 530004, China

Prof. Z. L. Wang, Prof. X. Pu  
CUSTech Institute  
Wenzhou, Zhejiang 325024, China

Prof. Z. L. Wang  
School of Materials Science and Engineering  
Georgia Institute of Technology  
Atlanta, GA 30332-0245, USA  
E-mail: zlwang@gatech.edu

 The ORCID identification number(s) for the author(s) of this article can be found under <https://doi.org/10.1002/adfm.202104348>.

DOI: 10.1002/adfm.202104348



**Scheme 1.** Scheme of the SC-ESCD. It integrates an electrochromic supercapacitor as both the optical responsive and energy storage device, and a DC-TENG as energy harvesting device.

power management circuits inevitable. Recently, direct current TENG (DC-TENG) has been reported by utilizing the coupled effects of contact electrification and dielectric breakdown, which is different from tribovoltaic effect.<sup>[35–38]</sup> It can obtain a higher output voltage, which makes it possible for simpler integration of self-charging power sources.<sup>[38–43]</sup>

Therefore, we propose here a self-charging ESCD (SC-ESCD) as shown in **Scheme 1**. A sliding-mode DC-TENG is integrated with an ESCD smart window. By sliding the DC-TENG on the window, the generated DC current will charge the ESCD, whose color will change then accordingly either for information display or for transmittance modulation. Therefore, the SC-ESCD can fulfill these two functions: i) an optical responsive device that can respond to sliding motion stimuli, and ii) self-charging power sources that could harvest, store and supply energy to other electronics. A solid-state ESCD based on polyaniline (PANI) was constructed, which exhibited an obvious coloring and discoloring phenomenon with a rapid response to the external

voltage. Simultaneously, the ESCD achieved high capacitance ( $15.2 \text{ mF cm}^{-2}$ ) and stable cycling performances (99% for 5000 cycles). Moreover, excellent flexibility was demonstrated for the ESCD. By integrating with a sliding DC-TENG, the SC-ESCD was able to change the display information without an extra power supply, and meantime the stored energy in the SC-ESCD can power other electronics. These self-charging power systems will have broad applications for next-generation smart electronics.

## 2. Result and Discussion

### 2.1. Fabrication of Solid-State Electrochromic Supercapacitors Device (ESCD)

In this study, conjugated polymer PANI was utilized as the electrochromic active materials in the ESCD. **Figure 1a** illustrates the fabrication procedure of the patterned PANI electrodes and

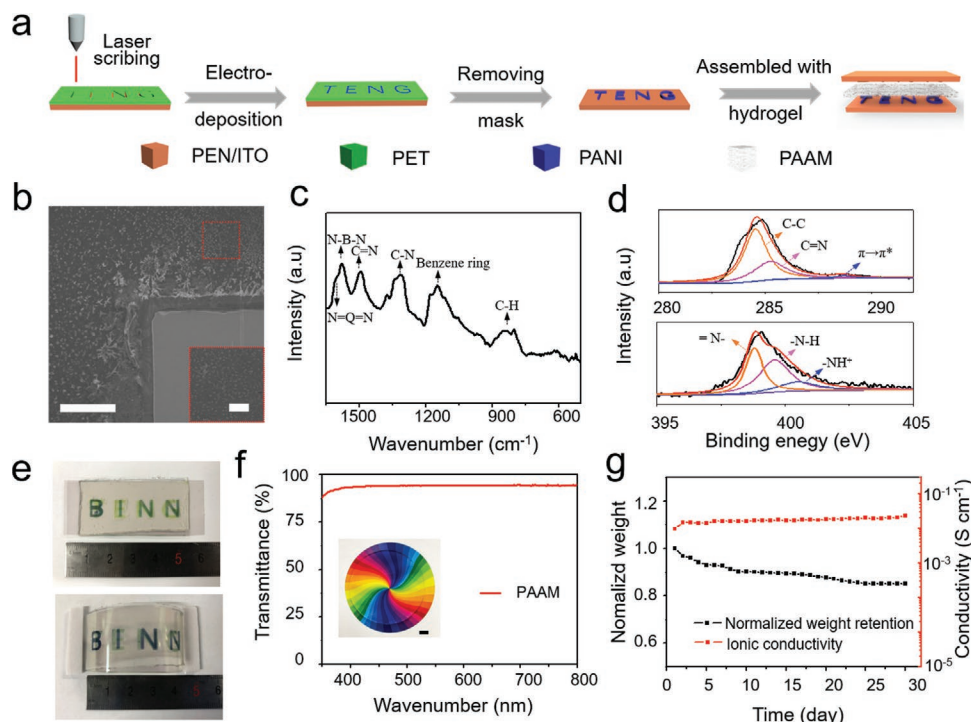


**Figure 1.** Fabrication of the patterned electrodes and solid-state ESCD. a) Schematic illustration of the fabrication process. b) SEM images, c) IR spectrum, d) XPS of C 1s and N 1s of the electrochemical polymerized PANI on PEN/ITO substrate. e) Photos of solid-state ESCD at flat (upper plot) and bend state (bottom plot). f) Transmittance in the visible range, g) ionic conductivity and water loss test of the PAAM-LiCl hydrogel. Inset of (f) is a photo of the hydrogel (scale bar: 2 cm). Scale bars, 200  $\mu\text{m}$  (b) and 1  $\mu\text{m}$  (inset of (b)).

the all-solid-state ESCD. Transparent conductive film of indium tin oxide (ITO) on flexible polyethylene-naphthalate (PEN) was used as the electrode substrate. With the aid of a laser-scribed PET film as the resistive template, a layer of PANI with desired patterns was electrodeposited only on the exposed ITO area. After detaching the PET, the patterned PANI electrodes were obtained. Subsequently, two identical PANI electrodes were attached on the two sides of the ionic hydrogel PAAm-LiCl electrolyte to assemble an all-solid-state ESCD. The PANI electrodes with 5 min electrodeposition (Figure 1b) exhibit a flat and dense surface with a clear boundary at the edge of the patterns. As shown in Figure S1 and S2, Supporting Information, longer electrodeposition time (10 and 30 min) leads to many particles aggregated with wrinkled or cracked surfaces, while longer electrodeposition time also results in thicker PANI layers. Figure 1c provides the reference Fourier transform infrared spectrum (FTIR) of the PANI. The prominent absorption bands situated at 802, 1147, 1312, 1493, 1581, and 1600  $\text{cm}^{-1}$  were attributed to the following vibration modes: bending of C–H (out-of-plane) on the benzene ring (B), bending of C–H (in-plane), mode of N=quinoid ring (Q)=N, stretching of Caromatic-N, stretching of N–B–N and stretching of N=Q=N, respectively.<sup>[44–46]</sup> The surface chemical compositions and the valence states were characterized by X-ray photoelectron spectroscopy (XPS). As shown in Figure 1d, the C 1s peak can be split into three peaks at 284.6, 285.4, and 288.7 eV, assigned to graphitized carbon (C–C), C=N,  $\pi$ - $\pi^*$  transition peak, respectively.<sup>[47,48]</sup> The N 1s core-level spectrum would be ascribed to quinonoid imine –N=) at 398.8 eV, benzenoid amine –NH–) at 399.6 eV, and nitrogen cationic radical –N<sup>+</sup>–) at 400.5 eV.<sup>[49,50]</sup> The above results confirmed that PANI was successfully grown on the ITO surface by electrochemical polymerization.

The solid-state hydrogel electrolyte for ESCD has to be flexible, transparent, ionic conductive, and stable in the atmosphere environment. Figure 1e shows the photo images of all-solid-state ESCD based on hydrogel electrolyte at flat (upper plot) and bent state (bottom plot). The hydrogel electrolyte showed an average transmittance of 94.5% in the visible range (wavelength 400 to 800 nm) (Figure 1f). To confirm its environmental stability, the weight and conductivity of the hydrogel were measured along time when it was kept at room temperature. As shown in Figure 1g, the weight of PAAm-LiCl hydrogel electrolyte decreased to 90% in the first ten days and then remained stable at  $\approx$ 85% over a month. The conductivity of the hydrogel increased slightly over time, possibly due to the thinning of the membrane and the rising salt concentration. Therefore, it was confirmed that the dehydration of the PAAm-LiCl hydrogel electrolyte was not serious at room temperature in atmosphere environment, which helps to solve the problems of water leakage and evaporation caused by the liquid electrolyte.

## 2.2. Electrochromic and Energy Storage Performances of the ESCD

The reaction mechanism and accompanying color change of the as-prepared PANI electrode were studied in a three-electrode system using 4 M LiCl aqueous solution as the electrolyte, Ag/AgCl as the reference electrode, and Pt sheet as the

counter electrode. The redox reaction of PANI was schematically explained in Figure S3, Supporting Information. At the potential of 0.8 V (versus Ag/AgCl), the PANI working electrode was at the anions ( $\text{Cl}^-$ ) doping state with dark blue color, and the oxidation state was dominating. While the applied external voltage was 0 V (versus Ag/AgCl), a leucoemeraldine state with yellow-green color was observed during the process of anions de-doping.<sup>[45,46]</sup> The transmission spectra for the PANI electrode and PEN/ITO background were obtained and shown in Figure 2a. In the visible range (400–800 nm), the PANI electrode at the bleached or reduced state (0 V versus Ag/AgCl) shows higher transmittance (average transmittance of 73.2%) and is light green (the inset photo); it changes to dark blue (52.4% of average transmittance) while at the colored or oxidized state (0.8 V versus Ag/AgCl). Additionally, the energy-dispersive X-ray spectroscopy spectrum and elemental mapping of PANI at different states further confirmed the doping and de-doping process of chloride ions (Figures S4 and S5, Supporting Information). The reason for the residual chlorine in the leucoemeraldine state is that the chlorine may not be completely de-doped from the PANI.

As shown in Figure 2b, the switching time of the patterned PANI electrode was measured by applying the constant potential of 0.8 or 0 V (versus Ag/AgCl). When a potential of 0.8 V was applied, the current decreased from 3.7 to 0.2 mA and then kept at 0.2 mA. A similar result can be observed when a potential of 0 V was applied. Moreover, it can be observed that the response time of coloration and bleaching are 1.4 and 1.5 s, respectively, indicating that the PANI electrode has a rapid response to the external voltage. For large-capacity PANI electrodes with a 30 min electroplating time (Figure S6, Supporting Information), the response time was also greatly extended (coloration with 10 s and bleaching with 7.8 s). Therefore, there is a trade-off between the electrochromic response time and the supercapacitor capacity (will be discussed below), and attention should be paid according to the specific applications of the ESCDs.

To further verify the electrochromic characteristics, the ESCD was fabricated into a sandwiched structure with the hydrogel electrolyte and two PANI electrodes in different patterns. Cyclic voltammetry (CV) scanning in the range of –0.8–0.8 V was applied to the two PANI electrodes. The patterned “BINN” electrode on the top exhibited a dark blue color at 0.8 V, which was bleached gradually to “blue  $\rightarrow$  green  $\rightarrow$  light green  $\rightarrow$  light yellow-green” when the voltage swiping to –0.8 V (Figure 2c). Meantime, the color of the bottom “TENG” electrode showed a reverse color change. Therefore, the ESCD showed letter of “BINN” clearly at 0.8 V, but the letters “TENG” at –0.8 V. Apart from the patterned alphabet, the PANI electrodes can be fabricated into other different shapes. A similar electrochromic process was observed for a “rabbit drawing” patterned ESCD (Figure 2d). Figure S7, Supporting Information, showed the color change of ESCDs using PANI electrodes with longer electrodeposition time. The ESCD at bent state also exhibited an obvious coloring and discoloration phenomenon, demonstrating excellent flexibility (Figure S8, Supporting Information).

The all-solid-state ESCD not only is an electrochromic device but combines energy storage and electrochromic functions. Therefore, electrochemical energy storage performances of

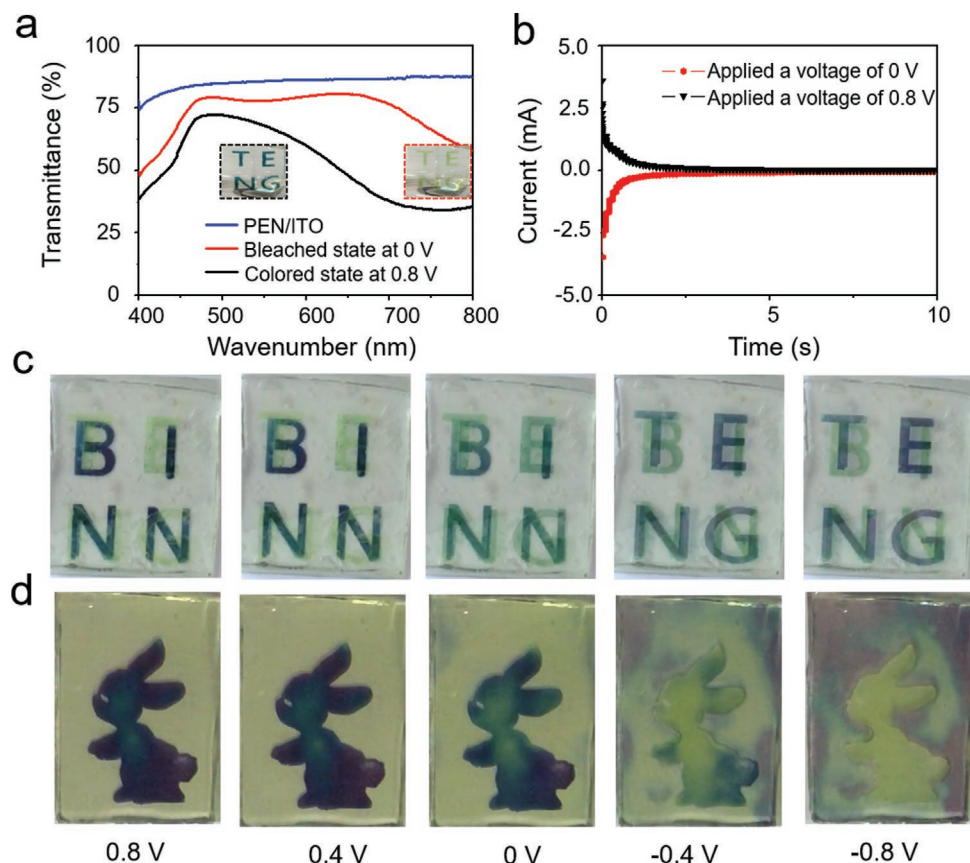


**Figure 2.** Electrochromic characterizations of solid-state ESCD. a) Transmittance spectra and b) chronoamperometry curves of ESCD under 0 V (bleached) and 0.8 V (colored). The inset of (a) are photos of ESCD at bleached (upper plot) and colored (bottom plot) states. c, d) Digital photos of the patterned all-solid-state ESCD showing different letters or patterns when different voltages are applied.

ESCD were evaluated. Solid-state ESCD were tested with two symmetric PANI electrodes as electrode and PAAm-LiCl as the gel-type electrolyte. The CV curves showed that the device exhibited stable electrochemical performance without  $\text{H}_2$  or  $\text{O}_2$  evolution when the potential window in the range  $-0.8$ – $0.8$  V (Figure 3a).<sup>[13,33]</sup> Figure 3b showed the typical CV curves between  $-0.8$  and  $0.8$  V at various scanning rates ranging from 10 to  $100 \text{ mV s}^{-1}$ . A pair of broad redox peaks at  $-0.2$  and  $0.2$  V was observed, which corresponded to the reduction/de-doping and the oxidation/doping process of the PANI.<sup>[45]</sup> Figure 3c showed the galvanostatic charge–discharge (GCD) curves under various current densities ranging from  $0.1$  to  $2 \text{ mA cm}^{-2}$ . The IR drop is 12, 55, and  $230 \text{ mV}$  at a current density of  $0.1$ ,  $0.5$ , and  $2 \text{ mA cm}^{-2}$ , respectively, indicating a good electrical conductivity of the electrodes. The areal discharge capacitance calculated by GCD curves at  $0.1 \text{ mA cm}^{-2}$  is  $2.55 \text{ mF cm}^{-2}$ , which remained to be  $1.8 \text{ mF cm}^{-2}$  after increasing the current density 20 times up to  $2 \text{ mA cm}^{-2}$  (Figure 3d). The corresponding specific capacitance was  $3.61 \text{ F g}^{-1}$  (considering PANI electrode mass). By tuning the electrodeposition time, the capacity can be controlled. Figure S9, Supporting Information, shows the CV and GCD curves of the PANI electrodes electrodeposited for 10 and 30 min. These results indicated excellent capacitive behaviors under a fast charge-discharge process, and the areal capacitances of PANI electrodes are increased with longer electrodeposition

times. Under the electroplating conditions of 10 and 30 min, its specific capacity is 6.2 and  $15.2 \text{ mF cm}^{-2}$  at  $0.1 \text{ mA cm}^{-2}$ , and maintained at 2.6 and  $7.0 \text{ mF cm}^{-2}$  at a current density of  $2 \text{ mA cm}^{-2}$ , respectively. Table S1, Supporting Information, summarized the specific capacities and electrochromic response times of the ESCD with different electrodeposition times. As mentioned above, a trade-off between the electrochromic response time and the supercapacitor capacity was confirmed. With the increasing electroplating time, the thickness and areal loading mass of the PANI will be increased, which lead to the lowered kinetics of the electrochemical reactions and the electrochromic response time will be sacrificed inevitably (Figure 2b and Figure S6, Supporting Information). Therefore, in order to obtain a compromised display effect and capacity storage performance, 5 min deposition time was used for PANI electrodes in following ESCDs, other than mentioned specifically.

Stable cycling performance was obtained, achieving capacitance retention of 99% after charging/discharging at  $0.1 \text{ mA cm}^{-2}$  for 5000 cycles (Figure 3e). The inset provided the GCD curves for the last 10 cycles of the charging-discharging process. A Ragone plot of the ESCD was provided in Figure 3f. The areal energy density of the ESCD was estimated to be  $0.64$ – $2.5 \mu\text{Wh cm}^{-2}$  at the areal power density of  $1.6 \text{ mW cm}^{-2}$ , generally much higher than or comparable with that of ESCDs based on Ag nanowires/ $\text{NiO}$ ,<sup>[14]</sup> Single-walled carbon nanotubes/PANI nanowires,<sup>[51]</sup>

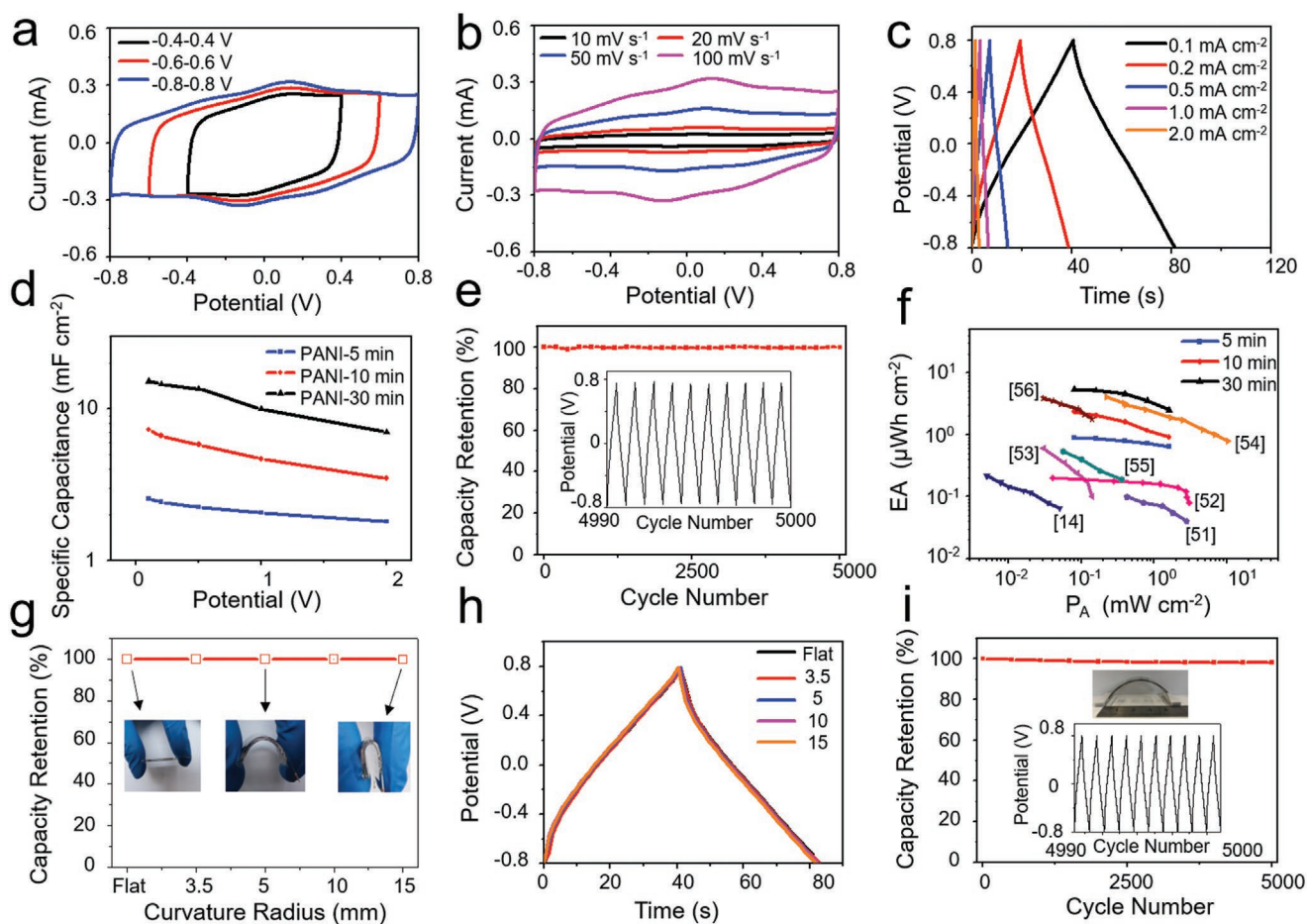


**Figure 3.** Energy storage performances of the all-solid-state ESCD. a) CV profiles of the ESCD with increasing potential windows. b) CV profiles of the ESCD with various scanning rates. c) GCD profiles of the ESCD with various current densities. d) The variation of specific areal capacitances of three ESCDs with different electrodeposition time. e) Cycling performance of the ESCD at a current density of  $0.1 \text{ mA cm}^{-2}$ . f) Ragone plot of the ESCDs in comparison with that of previously reported supercapacitors: Ag nanowires/ $\text{NiO}$ ,<sup>[14]</sup> Single-walled carbon nanotubes/PANI nanowires,<sup>[51]</sup> Multi-walled carbon nanotubes/ $\text{V}_2\text{O}_5$  nanowires,<sup>[52]</sup> 3D cellular graphene films,<sup>[53]</sup>  $\text{Ti}_3\text{C}_2$  MXene,<sup>[54]</sup>  $\text{Ni}/\text{MnO}_2$ ,<sup>[55]</sup> multiwalled carbon nanotubes/PANI,<sup>[56]</sup> g) capacitance retention and h) GCD curves of the ESCD with different bending radius at a current density of  $0.1 \text{ mA cm}^{-2}$ . i) Normalized capacitances of the device at a bending radius of 3.5 mm for 5000 cycles. The inset of (h,i) are photographs of an ESCD without and with various bending deformations.

Multi-walled carbon nanotubes/ $\text{V}_2\text{O}_5$  nanowires,<sup>[52]</sup> 3D cellular graphene films,<sup>[53]</sup>  $\text{Ti}_3\text{C}_2$  MXene,<sup>[54]</sup>  $\text{Ni}/\text{MnO}_2$ ,<sup>[55]</sup> and Multiwalled carbon nanotubes/PANI.<sup>[56]</sup>

In order to meet the specific energy requirements of higher voltage or capacitance in practical applications, the ESCD can be connected in series or parallel. As shown in Figure S10a, Supporting Information, two ESCDs connected in series showed the increased charging/discharging window to 1.6 V; while two ESCDs connected in parallel showed doubled charge/discharge time (Figure S10b, Supporting Information). These results were also consistent with the CV measurements in Figure S10c, Supporting Information. The mechanical flexibility and durability of flexible all-solid-state ESCD were also examined. There was no noticeable decrease in electrochemical performance even at a shallow bending radius of 3.5 mm (Figure 3g,h). In addition, the ESCD showed capacitance retention of 98% at bending radius of 3.5 mm after 5000 cycles of GCD tests (Figure 3i and the inset). These results suggested the exceptional energy storage performances and flexibility of the ESCDs.

### 2.3. Direct-Current Triboelectric Nanogenerator (DC-TENG)

In order to realize the self-charging ESCD, a DC-TENG based on coupled effects of contact electrification and dielectric breakdown was fabricated to convert the mechanical sliding motion into electricity.<sup>[38]</sup> The DC-TENG was composed of two parts: a PEN film as the tribo-electrification layer, and a slider with two Cu electrodes, as shown in Figure 4a. The electricity-generating mechanism is schematically illustrated as well. The contact electrification will occur at PEN-Cu interfaces when rubbing the bottom copper foil with the PEN. There are positive charges on the bottom copper foil and negative static charges on PEN caused by the triboelectrification effect (Figure 4a,i). When the slider moves to the right, a high electric field is formed between the side Cu electrode and the PEN layer. Furthermore, the side Cu electrode is designed to be in very thin thickness ( $65 \mu\text{m}$ ), so as to enlarge the electric field at the Cu electrode tip. Then, accompanying the accumulated static charges in the PEN, electric breakdown occurs when the electric field exceeds the dielectric strength

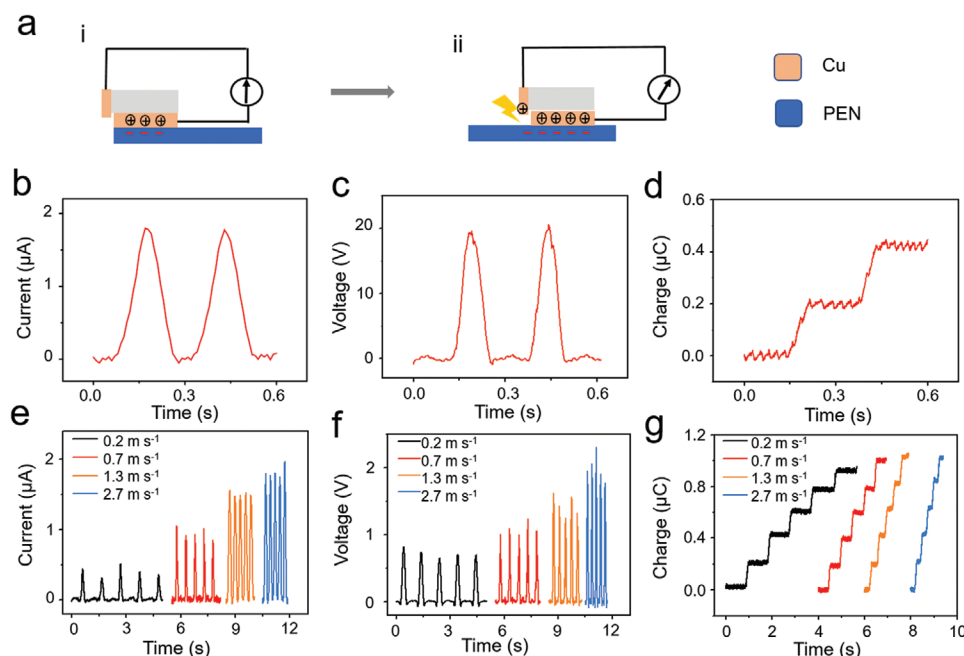


**Figure 4.** Working mechanism and output performance of the energy-harvesting DC-TENG. a) Schematic illustrations of the working mechanism of the DC-TENG. b) Short-circuit current ( $I_{sc}$ ), c) open-circuit voltage ( $V_{oc}$ ), and d) transferred charges ( $Q_{sc}$ ) of the sliding mode DC-TENG at average speed of  $2.7 \text{ m s}^{-1}$ . e)  $I_{sc}$ , f)  $Q_{sc}$ , and g)  $V_{oc}$  of the sliding mode DC-TENG at various average speeds.

of air. The air nearby the side Cu electrode will be ionized, and the electrons flow from the PEN surface to the side Cu electrode as well (Figure 4a(ii)). Finally, until the slider moves to the far right, the discharge will continue through the external circuit. Nevertheless, if the slider moves in the opposite direction, no current flows in the external circuit because there is not enough potential difference between the side Cu electrode and PEN right underneath to cause dielectric breakdown. Therefore, the repeated reciprocal sliding motions of the slider lead to the pulsed DC output.

Figure 4b–g shows the short-circuit current ( $I_{sc}$ ), open-circuit voltage ( $V_{oc}$ ), and transferred charge ( $Q_{sc}$ ) of the sliding-mode DC-TENG. The  $I_{sc}$  and  $V_{oc}$  have a peak value of about  $1.8 \mu\text{A}$  (Figure 4b) and  $20 \text{ V}$  (Figure 4c) at average speed of  $2.7 \text{ m s}^{-1}$ ; the  $Q_{sc}$  generated by one sliding motion is stable at  $200 \text{ nC}$  (Figure 4d). It is noticed that the  $Q_{sc}$  is independent of average speed because it is determined by the collected charge area after triboelectrification.<sup>[38,40]</sup> For the sliding motion, by increasing the motion average speeds, the amplitude of the  $I_{sc}$  increase from  $0.4 \mu\text{A}$  at  $0.2 \text{ m s}^{-1}$  to  $2 \mu\text{A}$  at  $2.7 \text{ m s}^{-1}$  (Figure 4e), and the  $V_{oc}$  also increases correspondingly, from  $8$  to  $20 \text{ V}$  (Figure 4f), while the amplitude of the  $Q_{sc}$  keeps almost unchanged (Figure 4g). The DC-TENG can sufficiently light up 33 blue LEDs in series by sliding the slider (Figure S11, Supporting Information). Moreover, the output current shows no obvious degradation after 5000 cycles at average speed of  $2.7 \text{ m s}^{-1}$  (Figure S12, Supporting Information).

#### 2.4. Self-charging Electrochromic Supercapacitor Device (SC-ESCD)

SC-ESCD was designed then by integrating the DC-TENG and the ESCD, as shown in Figure 5a. The DC-TENG and the ESCD share the same PEN film. One PEN substrate of the ESCD is

used as the tribo-electrification layer of the DC-TENG, and the slider can just slide on top of the ESCD. The two electrodes of the DC-TENG will be connected to the ESCD directly without using rectifying or conditioning circuits. The optical photo of the final self-charging electrochromic device is shown in Figure 5b. Due to the size limitation of the electrochromic supercapacitor (approximately  $6 \times 2 \text{ cm}^2$ ), the slider size of the DC-TENG was reduced to  $1 \times 1 \text{ cm}^2$ . Figure S13, Supporting Information, exhibits the output of short-circuit current ( $I_{sc}$ ), and short-circuit transferred charge ( $Q_{sc}$ ) of small-sized DC-TENG. Considering the lowered outputs of the DC-TENG due to the reduced size, we also reduced the electrodeposition time of PANI to 2 min. The typical CV, GCD curves, and the switching time of the ESCD were shown in Figures S14, S15, and Table S1.

The equivalent circuit of the SC-ESCD system was shown in Figure 5c. The self-charging capability was verified by charging the ESCD when continuously sliding the slider. As shown by the voltage profile in Figure 5d and the correspondent photos in Figure 5e, the ESCD can be charged to  $0.8 \text{ V}$  in  $430 \text{ s}$  at average speed of  $2.7 \text{ m s}^{-1}$  and the ESCD showed letters of “BINN” as the top “BINN” patterned electrode was at doped state. Then, the ESCD was discharged to  $0 \text{ V}$  at a constant current of  $50 \mu\text{A}$  for  $35 \text{ s}$ , and the clear letter pattern became blurred accordingly. Finally, we reversed the connection between the DC-TENG and ESCD for a reverse self-charging process. The letters of “TENG” were clearly observed after the ESCD was reversely self-charged to  $0.8 \text{ V}$ . These results showed that the SC-ESCD can respond to sliding motion for different information display, and electric charges are stored in the ESCD during the sliding-triggered electrochromic process.

Lastly, the application of the SC-ESCD as a self-charging power source was demonstrated. Two ESCDs were connected in series, which can be charged by the DC-TENG to  $1.6 \text{ V}$  in  $15 \text{ min}$  and then power an electronic watch for  $3.4 \text{ min}$  (Figure 5f).

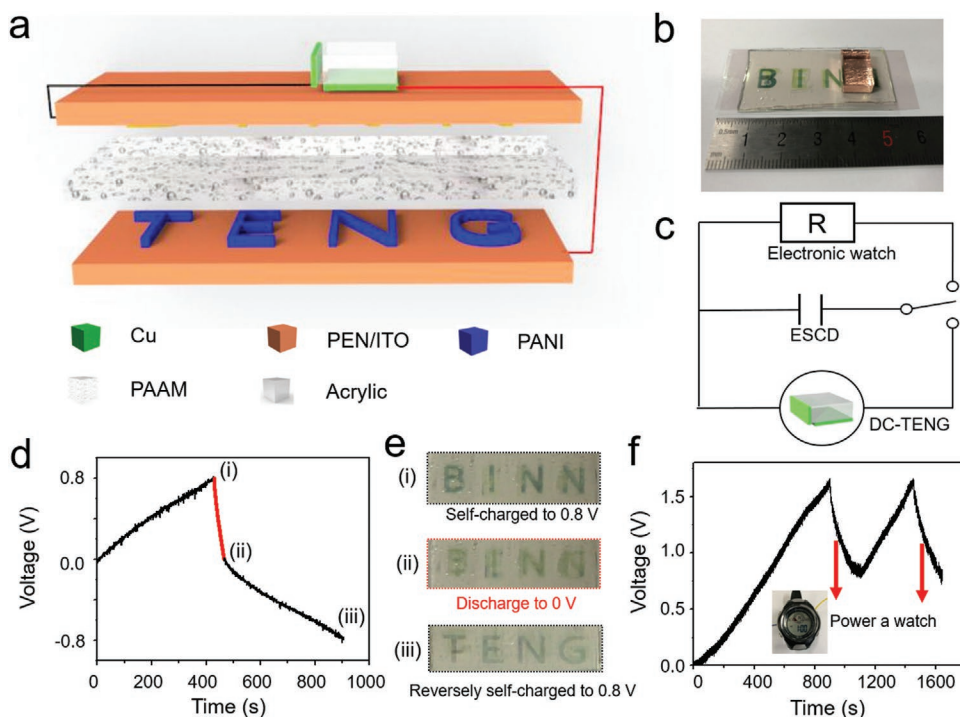


**Figure 5.** An SC-ESCD. a) Schematic illustration, b) a photo, and c) an equivalent circuit of the SC-ESCD, which integrates the energy harvesting DC-TENG and the ESCD. d) Voltage profiles of the ESCD when being self-charged to 0.8 V by sliding motions, discharged to 0 V using a constant current (50  $\mu$ A), and then reversely self-charged to 0.8 V. e) Photographs of the ESCD at various states in accordance to (d). f) Voltage profile of two series-connected ESCDs being charged by the sliding DC-TENG and then discharged by powering a watch (inset photo).

Subsequently, the ESCD can be charged back to 1.6 V, and the watch can be repeatedly powered. These results confirmed that the SC-ESCD can respond to sliding stimuli for color change or display information change, and simultaneously can be applied as a power source to power personal electronics without extra power devices.

### 3. Conclusion

In summary, the all-solid-state SC-ESCD with both abilities as self-charging power sources and rapid optical responsive devices has been successfully fabricated. The integrated SC-ESCD was able to display obvious color change under a sliding state and without extra power supply, and meantime harvest, store, and energy supply to other electronics. Flexibility of the SC-ESCD was also demonstrated. In addition, thanks to the stability and planar structure of the SC-ESCD, it can also be prepared into arbitrary shapes according to possibly diverse needs. The DC-TENG in the SC-ESCD can obtain constant current output without rectification, which facilitated the integration system. This self-charging power systems have potential applications in multifunctional smart displays, touch screens, or electronic tags.

### 4. Experimental Section

**Fabrication of PANI Electrode:** PEN-ITO (polyethylene-naphthalate-Indium Tin Oxide) was carefully cleaned with acetone, ethanol, and

distilled water in an ultrasonic bath for 30 min. Subsequently, PANI was deposited on the bare conductivity ITO under constant current of 0.1 mA  $\text{cm}^{-2}$  for 2, 5, 10, and 30 min in a solution of  $\text{Na}_2\text{SO}_4$  (0.5 M),  $\text{H}_2\text{SO}_4$  (0.5 M), and aniline (0.05 M) using Ag/AgCl as the reference electrode and Pt sheet as the counter electrode. The mass loading of active materials on the PEN/ITO is measured to 0.6–1.5 mg  $\text{cm}^{-2}$  with 5 min electrodeposition time. Finally, the obtained sample was washed with deionized water and air-dried.

**Fabrication of the All-Solid-State ESCD:** The PAAm-LiCl hydrogel was achieved as described in the previously reported references.<sup>[57]</sup> Briefly, acrylamide powder (14 weight % relative to deionized water) was dispersed in the 4 M LiCl aqueous solution. Then, *N,N'*-methylenebisacrylamide, ammonium persulfate, and *N,N,N',N'*-tetramethylethylenediamine were added to the solution consecutively under magnetic stir. The solution was subsequently transferred into a glass mold and treated at 50  $^{\circ}\text{C}$  for 2 h to form the PAAm-LiCl hydrogel. The thickness of PAAm-LiCl hydrogel is about 2.4 mm. Finally, the ESCD device was assembled by covering two PANI electrodes on the sides of PAAm-LiCl hydrogel.

**Fabrication of the DC-TENGs:** The DC-TENGs were achieved in the previously reported references.<sup>[38]</sup> Typically, a specific size of acrylic sheets was cut out by a laser machine cutter and used as a substrate. (PLS6.75, Universal Laser Systems). Then, PEN film was used as the tribo-electrification layer and flatly attached to the acrylic sheets (20  $\times$  6  $\times$  0.4 cm). Subsequently, the copper foil (65  $\mu\text{m}$ ) was affixed to the left and below of the acrylic sheets (1  $\times$  5  $\times$  0.4 cm, 1  $\times$  1  $\times$  0.4 cm).

**Characterization:** The sample morphologies were characterized by field emission scanning electron microscopy (FESEM, Hitachi SU8200). FTIR spectra were taken by a TENSOR II spectrometer (BRUKER, VERTEX80v). The transmittance was performed with a UV3600 spectrophotometer. The electrochemical performance was measured by an electrochemical work station (CHI 760E). The output short current and open-circuit voltage of the TENG were measured by a Keithley electrometer (Keithley 6514).



The capacitances ( $C_a$ , F cm<sup>-2</sup>) from GCD discharging curves can be calculated according to the following equations.

$$C_a = \frac{Q}{\Delta U} = \frac{i\Delta t}{\Delta U} \quad (1)$$

$$C_a = \frac{It}{U} \quad (2)$$

The parameters of  $Q$ ,  $i$ ,  $t$ ,  $A$ , and  $U$  are presented as average charge, discharging current, discharge time, effective area of electrode, and potential window, respectively.

The energy density ( $E_a$ , Wh cm<sup>-2</sup>) and average power density ( $P_a$ , W cm<sup>-2</sup>) were calculated based on the following equations.

$$E_a = \frac{1}{2} \times C_a \times \frac{U^2}{3600} \quad (3)$$

$$P_a = \frac{3600 \times E_a}{t} \quad (4)$$

## Supporting Information

Supporting Information is available from the Wiley Online Library or from the author.

## Acknowledgements

W.G. and Z.C. contributed equally to this work. The authors thank the support from the National Key Research and Development Program of China (2016YFA0202703, 2016YFA0202702), the National Natural Science Foundation of China (Grant Nos. 51432005, 61574018, and 51603013), the Youth Innovation Promotion Association of CAS, and "Hundred Talents Program" of CAS.

## Conflict of Interest

The authors declare no conflict of interest.

## Data Availability Statement

Research data are not shared.

## Keywords

electrochromic supercapacitors, energy harvesting, self-charging power systems, smart windows, triboelectric nanogenerators

Received: May 8, 2021

Revised: June 6, 2021

Published online:

[1] J. Chen, Y. Huang, N. Zhang, H. Zou, R. Liu, C. Tao, X. Fan, Z. L. Wang, *Nat. Energy* **2016**, 1, 16138.

[2] L. Hu, Y. Cui, *Energy Environ. Sci.* **2012**, 5, 6423.

[3] Y. Qin, X. Wang, Z. L. Wang, *Nature* **2009**, 457, 340.

[4] P. Yang, P. Sun, Z. Chai, L. Huang, X. Cai, S. Tan, J. Song, W. Mai, *Angew. Chem., Int. Ed.* **2014**, 53, 11935.

[5] T. G. Yun, M. Park, D. H. Kim, D. Kim, J. Y. Cheong, J. G. Bae, S. M. Han, I. D. Kim, *ACS Nano* **2019**, 13, 3141.

[6] R. Kunwar, M. Harilal, S. G. Krishnan, B. Pal, I. I. Misnon, C. R. Mariappan, F. I. Ezema, H. I. Elim, C.-C. Yang, R. Jose, *Adv. Fiber Mater.* **2019**, 1, 205.

[7] S. Zhang, S. Cao, T. Zhang, A. Fisher, J. Y. Lee, *Energy Environ. Sci.* **2018**, 11, 2884.

[8] D. Mandal, P. Routh, A. K. Nandi, *Small* **2018**, 14, 1702881.

[9] T. Xu, X. Li, Z. Liang, V. S. Amar, R. Huang, R. V. Shende, H. Fong, *Adv. Fiber Mater.* **2020**, 2, 74.

[10] C. Ye, Q. Xu, J. Ren, S. Ling, *Adv. Fiber Mater.* **2019**, 2, 24.

[11] M. Qiu, P. Sun, B. Zhang, J. Yu, Y. Fu, X. Yu, C. Zhao, W. Mai, *Adv. Optical Mater.* **2018**, 6, 1800338.

[12] L. Shen, L. Du, S. Tan, Z. Zang, C. Zhao, W. Mai, *Chem. Commun.* **2016**, 52, 6296.

[13] Y. Zhong, Z. Chai, Z. Liang, P. Sun, W. Xie, C. Zhao, W. Mai, *ACS Appl. Mater. Interfaces* **2017**, 9, 34085.

[14] S. Qin, Q. Zhang, X. Yang, M. Liu, Q. Sun, Z. L. Wang, *Adv. Energy Mater.* **2018**, 8, 1800069.

[15] X. Pu, L. Li, M. Liu, C. Jiang, C. Du, Z. Zhao, W. Hu, Z. L. Wang, *Adv. Mater.* **2016**, 28, 98.

[16] X. Pu, M. Liu, L. Li, S. Han, X. Li, C. Jiang, C. Du, J. Luo, W. Hu, Z. L. Wang, *Adv. Energy Mater.* **2016**, 6, 1601254.

[17] S. Chen, Z. Wang, H. Ren, Y. Chen, W. Yan, C. Wang, B. Li, J. Jiang, C. Zou, *Sci. Adv.* **2019**, 5, eaav6815.

[18] C. J. Barile, D. J. Slotcavage, J. Hou, M. T. Strand, T. S. Hernandez, M. D. McGehee, *Joule* **2017**, 1, 133.

[19] R. T. Wen, C. G. Granqvist, G. A. Niklasson, *Nat. Mater.* **2015**, 14, 996.

[20] W. Zhang, X. Wang, Y. Wang, G. Yang, C. Gu, W. Zheng, Y. M. Zhang, M. Li, S. X. Zhang, *Nat. Commun.* **2019**, 10, 1559.

[21] J. Wang, C. Meng, Q. Gu, M. C. Tseng, S. T. Tang, H. S. Kwok, J. Cheng, Y. Zi, *ACS Nano* **2020**, 14, 3630.

[22] J. Wang, C. Meng, C.-T. Wang, C.-H. Liu, Y.-H. Chang, C.-C. Li, H.-Y. Tseng, H.-S. Kwok, Y. Zi, *Nano Energy* **2021**, 85, 105976.

[23] T. Ye, Y. Sun, X. Zhao, B. Lin, H. Yang, X. Zhang, L. Guo, *J. Mater. Chem. A* **2018**, 6, 18994.

[24] N. C. Davy, M. Sezen-Edmonds, J. Gao, X. Lin, A. Liu, N. Yao, A. Kahn, Y.-L. Loo, *Nat. Energy* **2017**, 2, 17104.

[25] T. G. Yun, D. Kim, Y. H. Kim, M. Park, S. Hyun, S. M. Han, *Adv. Mater.* **2017**, 29, 1606728.

[26] B. Tian, X. Zheng, T. J. Kempa, Y. Fang, N. Yu, G. Yu, J. Huang, C. M. Lieber, *Nature* **2007**, 449, 885.

[27] P. Dong, M.-T. F. Rodrigues, J. Zhang, R. S. Borges, K. Kalaga, A. L. M. Reddy, G. G. Silva, P. M. Ajayan, J. Lou, *Nano Energy* **2017**, 42, 181.

[28] Y. Fu, H. Wu, S. Ye, X. Cai, X. Yu, S. Hou, H. Kafafy, D. Zou, *Energy Environ. Sci.* **2013**, 6, 805.

[29] S. Niu, Z. L. Wang, *Nano Energy* **2015**, 14, 161.

[30] Z. L. Wang, J. Chen, L. Lin, *Energy Environ. Sci.* **2015**, 8, 2250.

[31] X. He, Y. Zi, H. Guo, H. Zheng, Y. Xi, C. Wu, J. Wang, W. Zhang, C. Lu, Z. L. Wang, *Adv. Funct. Mater.* **2017**, 27, 1604378.

[32] G. Zhu, Z. H. Lin, Q. Jing, P. Bai, C. Pan, Y. Yang, Y. Zhou, Z. L. Wang, *Nano Lett.* **2013**, 13, 847.

[33] M. Liu, Z. Cong, X. Pu, W. Guo, T. Liu, M. Li, Y. Zhang, W. Hu, Z. L. Wang, *Adv. Funct. Mater.* **2019**, 29, 1806298.

[34] X. Pu, W. Song, M. Liu, C. Sun, C. Du, C. Jiang, X. Huang, D. Zou, W. Hu, Z. L. Wang, *Adv. Energy Mater.* **2016**, 6, 1601048.

[35] S. Lin, Y. Lu, S. Feng, Z. Hao, Y. Yan, *Adv. Mater.* **2019**, 31, 1804398.

[36] S. Lin, R. Shen, T. Yao, Y. Lu, S. Feng, Z. Hao, H. Zheng, Y. Yan, E. Li, *Adv. Sci.* **2019**, 6, 1901925.

[37] Z. L. Wang, A. C. Wang, *Mater. Today* **2019**, 30, 34.

[38] D. Liu, X. Yin, H. Guo, L. Zhou, X. Li, C. Zhang, J. Wang, Z. L. Wang, *Sci. Adv.* **2019**, 5, eaav6437.

- [39] M. K. Gupta, J.-H. Lee, K. Y. Lee, S.-W. Kim, *ACS Nano* **2013**, *7*, 8932.
- [40] J. Luo, L. Xu, W. Tang, T. Jiang, F. R. Fan, Y. Pang, L. Chen, Y. Zhang, Z. L. Wang, *Adv. Energy Mater.* **2018**, *8*, 1800889.
- [41] J. Liu, A. Goswami, K. Jiang, F. Khan, S. Kim, R. McGee, Z. Li, Z. Hu, J. Lee, T. Thundat, *Nat. Nanotechnol.* **2018**, *13*, 112.
- [42] J. Wang, H. Wang, X. Li, Y. Zi, *Nano Energy* **2019**, *66*, 104140.
- [43] G. Xu, D. Guan, X. Yin, J. Fu, J. Wang, Y. Zi, *EcoMat* **2020**, *2*, 12037.
- [44] Z. Niu, P. Luan, Q. Shao, H. Dong, J. Li, J. Chen, D. Zhao, L. Cai, W. Zhou, X. Chen, S. Xie, *Energy Environ. Sci.* **2012**, *5*, 8726.
- [45] J. Sun, X. Pu, C. Jiang, C. Du, M. Liu, Y. Zhang, Z. Liu, J. Zhai, W. Hu, Z. L. Wang, *Sci. Bull.* **2018**, *63*, 795.
- [46] B. He, Q. Tang, T. Liang, Q. Li, *J. Mater. Chem. A* **2014**, *2*, 3119.
- [47] X. Liu, Z. Wu, Y. Yin, *Chem. Eng. J.* **2017**, *323*, 330.
- [48] J. Zhang, J. Jiang, H. Li, X. S. Zhao, *Energy Environ. Sci.* **2011**, *4*, 4009.
- [49] W. Chen, R. B. Rakhi, H. N. Alshareef, *Nanoscale* **2013**, *5*, 4134.
- [50] L. Wang, X. Feng, L. Ren, Q. Piao, J. Zhong, Y. Wang, H. Li, Y. Chen, B. Wang, *J. Am. Chem. Soc.* **2015**, *137*, 4920.
- [51] Q. Meng, K. Wang, W. Guo, J. Fang, Z. Wei, X. She, *Small* **2014**, *10*, 3187.
- [52] D. Kim, K. Keum, G. Lee, D. Kim, S.-S. Lee, J. S. Ha, *Nano Energy* **2017**, *35*, 199.
- [53] Y. Shao, J. Li, Y. Li, H. Wang, Q. Zhang, R. B. Kaner, *Mater. Horiz.* **2017**, *4*, 1145.
- [54] N. Kurra, B. Ahmed, Y. Gogotsi, H. N. Alshareef, *Adv. Energy Mater.* **2016**, *6*, 1601372.
- [55] Y. Chen, X. Li, Z. Bi, G. Li, X. He, X. Gao, *Chem. Eng. J.* **2018**, *353*, 499.
- [56] L. Li, C. Fu, Z. Lou, S. Chen, W. Han, K. Jiang, D. Chen, G. Shen, *Nano Energy* **2017**, *41*, 261.
- [57] X. Pu, M. Liu, X. Chen, J. Sun, C. Du, Y. Zhang, J. Zhai, W. Hu, Z. L. Wang, *Sci. Adv.* **2017**, *3*, e1700015.